Journal of Power Sources 196 (2011) 8644–8650

Contents lists available at ScienceDirect

Journal of Power Sources

journal homepage: www.elsevier.com/locate/jpowsour

Highly ordered lamellar V_2O_3-based hybrid nanorods towards superior aqueous lithium-ion battery performance

Yongfu Sun, Shishi Jiang, Wentuan Bi, Changzheng Wu, Yi Xie*

Hefei National Laboratory for Physical Sciences at Microscale, University of Science & Technology of China, Hefei, Anhui 230026, PR China

ARTICLE INFO

Article history:
Received 23 February 2011
Received in revised form 2 May 2011
Accepted 15 June 2011
Available online 22 June 2011

Keywords:
Ordered
Lamellar
Vanadium trioxide
Nanorods
Aqueous lithium-ion battery

ABSTRACT

Lithium-ion batteries with green and inexpensive aqueous electrolytes solve the safety problem associated with conventional lithium-ion batteries that use highly toxic and flammable organic solvents, which usually cause fires and explosions. However, the relatively low capacities (usually < 65 mAh g^{-1}) and less than 50% capacity retention over 50 cycles unfortunately limit their promising applicability. Herein, a novel model of ordered lamellar organic–inorganic hybrid nanorods is first put forward as an excellent platform to circumvent the above issues. Taking the synthetic highly ordered lamellar V_2O_3-based hybrid nanorods as an example, they deliver a capacity up to 131 mAh g^{-1}, nearly 1.5 and 2 times higher than that of 10-nm V_2O_3 nanocrystals (90 mAh g^{-1}) and 2-μm bulk V_2O_3 (73.9 mAh g^{-1}). Also, their excellent cyclability of 88% after 50 cycles is remarkably better than that of 10-nm V_2O_3 nanocrystals (64%) and 2-μm bulk V_2O_3 (41%). This work provides a facile route for gram-scale synthesizing highly ordered lamellar hybrid materials and proves that these unique structures are excellent platforms for significantly improving aqueous lithium-ion battery performances especially at high discharge rates, giving tantalizing perspectives in future design and synthesis of high-performance active materials for aqueous lithium-ion batteries.

1. Introduction

Since the early 1990s, rechargeable lithium-ion batteries with non-aqueous electrolytes have been widely used in portable equipments [1]. Although the performances of non-aqueous lithium-ion batteries are often satisfactory, their practical applications are still handicapped by the high cost and severe safety problems arising from the use of highly toxic and flammable solvents, which might cause fires and explosion [2]. In exploring new types of alternative battery systems with high safety and low cost, aqueous lithium-ion batteries have attracted much attention [3–6]. Since this new type of lithium-ion batteries utilizes aqueous electrolytes, they fundamentally resolve the safety problem resulting from organic electrolytes and avoid rigorous assembly conditions [4]. In addition to possessing high safety, low cost and environmental friendliness, the fascination also comes from their electrolytes affording two orders of magnitude higher ion conductivity than those of non-aqueous systems [7,8]. Despite these excellent advantages, the relatively low capacities (usually < 65 mAh g^{-1}) associated with less than 50% capacity retention over 50 cycles unfortunately hinder their promising applicability [3,5,9,10]. Thus, further breakthroughs in the design and synthesis of novel electrode materials, with high specific capacities and stable cycling life, hold the key to the development of aqueous lithium-ion batteries.

Herein, we first put forward a novel and ideal model system of ordered lamellar organic–inorganic hybrid nanorods as an excellent platform to circumvent the above issues. This designed geometry has several tantalizing advantages in enhancing the capacity and cycling life of aqueous lithium-ion batteries, as illustrated in Scheme 1a. Within these hybrids, the organic component can be used to tailor the electronic properties of inorganic framework by defining its reduced dimensionality and mediating the electronic coupling between inorganic unites [11]. In this case, the use of dimensionally confined ultrathin inorganic layers as lithium hosts helps to shorten the lithium ion diffusion length and enhance the surface area contact with electrolyte, thus contributing to achieve faster kinetics and higher capacity [12,13]. Also, the ultrathin inorganic components allow for facile strain relaxation without fracture and shedding that occur in bulk or micron-sized materials (Scheme 1c) so that much more stable cycling life can be achieved [14]. Moreover, the rod-like configuration has direct one-dimensional (1D) electrical pathways facilitating efficient charge transport [15], whereas the electronic charge carriers

* Corresponding author. Tel.: +86 551 3603987; fax: +86 551 3606266.
E-mail address: yxie@ustc.edu.cn (Y. Xie).

0378-7753/$ – see front matter © 2011 Elsevier B.V. All rights reserved.
doi:10.1016/j.jpowsour.2011.06.050

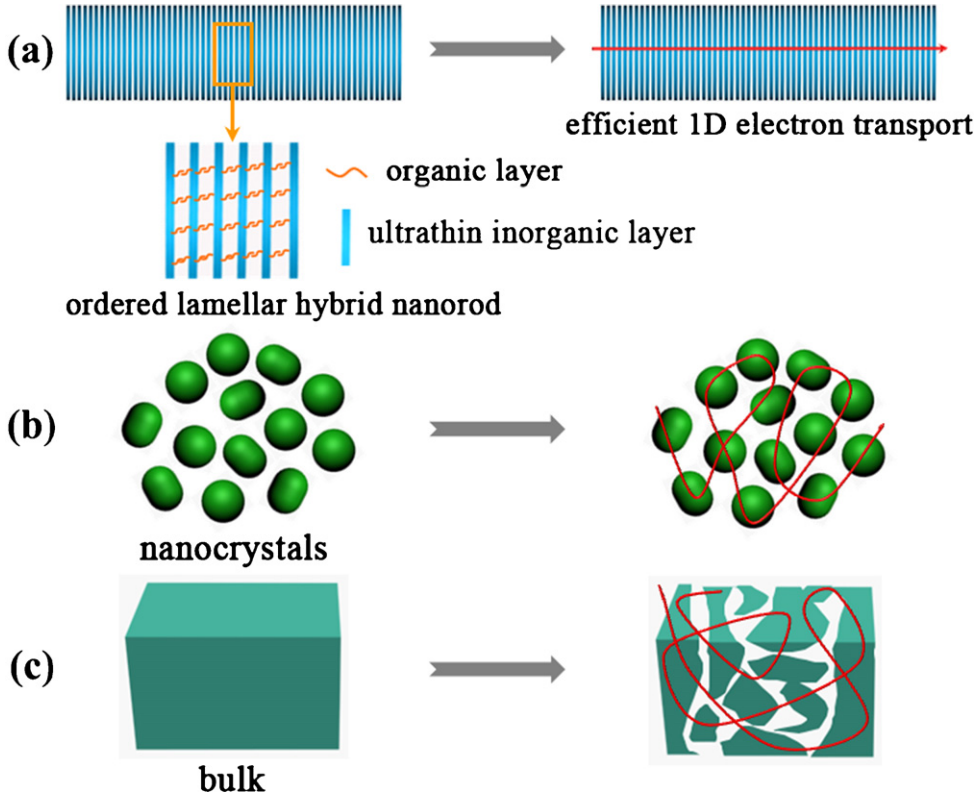

Scheme 1. Electron transport pathway (indicated by red line) and morphological change that occur in different structured electrode materials during electrochemical cycling: (a) ordered lamellar hybrid nanorod consists of ultrathin inorganic layers, regularly separated from each other by intercalated organic molecules. Advantages of this novel electrode include efficient 1D electron transport, facile strain relaxation, short lithium insertion distance, large contact area with electrolyte, extra lithium storage space and easy electrolyte infiltration. (b) Nanocrystals do not pulverize into smaller particles after cycling thanks to their facile strain relaxation, but the disconnected particles increase transport distance of electrons and lithium ions. (c) Large volume expansion in bulk materials leads to their pulverization and shedding during cycling. The cracked particles increase transport distance of electrons and lithium ions, while the loss of active materials decreases specific capacity. (For interpretation of the references to color in this figure legend, the reader is referred to the web version of the article.)

must move through the interparticle contact area in the disconnected nanocrystals or cracked bulk materials (Scheme 1b and c). Furthermore, the large interlayer distance between inorganic layers not only provides easy electrolyte infiltration and extra storage space for lithium ions but also acts as an elastic zone to buffer volume change during lithium uptake-release [16,17], thereby maintaining good electronic contact and guaranteeing excellent powder performance.

As is well-known, good conductivity is a prerequisite for an excellent electrode material. In this regard, atomic structural analysis gives us inspiration that rhombohedral V_2O_3 seems to be an appealing candidate for the desirable electrode material. As shown in Fig. 1a, the rhombohedral V_2O_3 possesses a 3-dimensional V–V framework where the V3d electrons could itinerate along the V–V chains [18], thus rendering it to take on an intrinsic metallic behavior which is further verified by the simulation on its band structure and density-of-states (Fig. S1). More strikingly, the presence of tunneled structures in rhombohedral V_2O_3 (Fig. 1b–d) facilitates the intercalation/deintercalation of lithium ions and endows it with a theoretical capacity as high as 356 mAh g^{-1} [19,20], which makes it particularly suitable as an active material for aqueous lithium-ion batteries where the capacity is a big concern. Inspired by the aforementioned concepts, highly ordered lamellar hybrid nanorods consisting of ultrathin V_2O_3 layers with thickness of 0.65 nm, regularly separated from each other by organic phenylacetate layers, are first successfully synthesized on a gram-scale via a novel and facile pathway and then introduced as the aqueous lithium-ion battery electrode, in efforts to achieve greatly enhanced capacity and cyclability.

2. Experimental

2.1. Synthesis of highly ordered lamellar V_2O_3-based hybrid nanorods

1.0 mL $VOCl_3$ was added into 80 mL phenethyl alcohol. After vigorous stirring for 30 min, the mixture was transferred into a 100 mL Teflon-lined autoclave, sealed and heated at 220 °C for 48 h. After cooling to room temperature naturally, the final product was collected by centrifuging the mixture, washed with dichloromethane and absolute ethanol for several times, and then dried in vacuum overnight for further characterization.

2.2. Characterization

XRD patterns were recorded by using a Rigaku TTR-III diffractometer with Cu Kα radiation (λ = 1.54178 Å). The FE-SEM images were performed by using a FEI Sirion-200 SEM. The TEM images were performed by using a JEOL-2010 TEM with an acceleration voltage of 200 kV. X-ray photoelectron spectra (XPS) were acquired on an ESCALAB MKII with Mg Kα ($h\upsilon$ = 1253.6 eV) as the excitation source. The binding energies obtained in the XPS spectral analysis were corrected for specimen charging by referencing C 1s to 284.5 eV. The IR spectra were measured on a NICOLET FT-IR spectrometer, using pressed KBr tablets. Inductively coupled plasma atomic emission spectrometry (ICP-AES) was performed on an Atomscan Advantage (Thermo Jarrell Ash Corporation (USA)). Elemental analysis was carried out on a Vario EL III (Elementar Analysensysteme, Germany). Thermal gravimetric analysis (TGA) of the as-synthesized sample was carried out on a NETZSCH TG 209

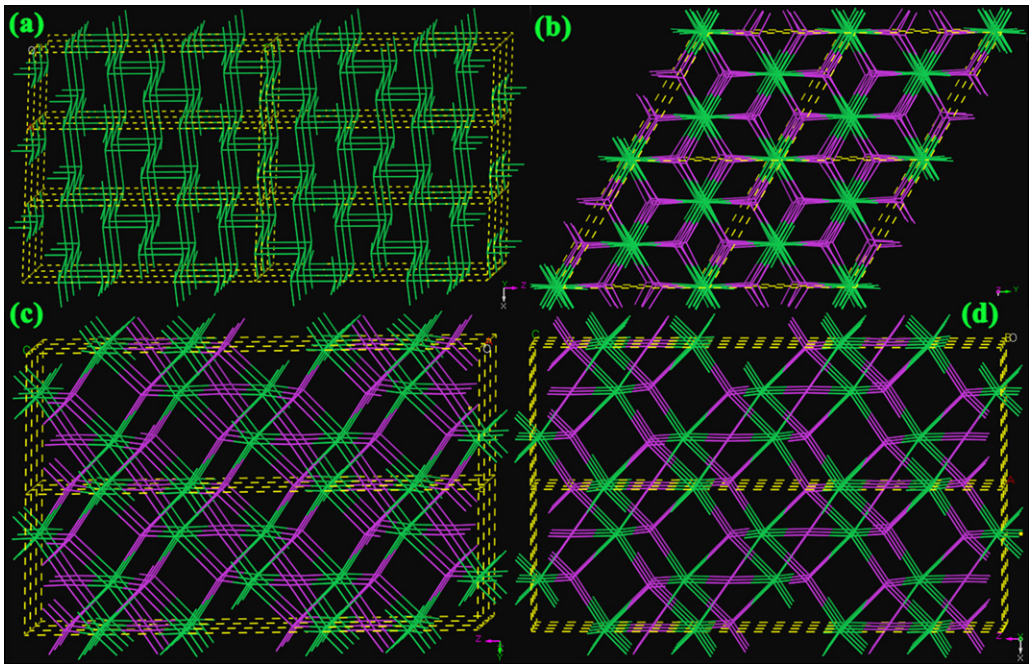

Fig. 1. (a) 3D V–V chains of $3 \times 3 \times 2$ supercell structure, (b) $2 \times 2 \times 2$ supercell structure projected along the Z axis, (c) $3 \times 2 \times 1$ supercell structure projected along the X axis and (d) $2 \times 3 \times 2$ supercell structure projected along the Y axis for rhombohedral V_2O_3, respectively. Tunneled structures can be clearly seen from b, c and d. The V atom locates at the cross point of green lines, while the intersection point of magenta lines stands for the O atom.

F3 thermal analyzer from room temperature to 600 °C at a heating rate of 10 °C min^{-1} in N_2.

2.3. Electrochemical measurements

All electrochemical measurements were performed at ambient temperature. The electrochemical performance of the samples for aqueous lithium-ion batteries was evaluated using a Teflon cell, where the excess $LiMn_2O_4$ was conducted in order to precisely evaluate the electrochemical capability of the synthetic samples. The preparation of negative and positive electrodes was conducted in a similar way. The electrode was prepared by pressing the mixture of sample/acetylene black/poly (vinylidene fluoride) (PVDF) with weight ratio of 70/20/10. The electrolyte was the aqueous solution including 5 M $LiNO_3$ and 0.001 M LiOH. The discharge and charge tests for aqueous lithium-ion batteries were carried out using Land battery system (CT2001A) at a constant current density with a cutoff voltage of 1.5–0.3 V.

3. Results and discussion

The X-ray diffraction (XRD) patterns in Fig. 2a and b displayed the information about the mesostructural order and the crystalline phase. In one aspect, the series of small-angle XRD peaks in Fig. 2a could be assigned to "0 0 L" ($L = 1, 2, 3, 4$, etc.), giving direct evidence for the presence of ordered mesostructure with a layer spacing of 1.94 nm. The higher orders, even the tenth at $2\theta = 47.5°$, were also visible on the wide-angle XRD pattern and denoted as asterisks in Fig. 2b, clearly demonstrating the high degree of order of the mesostructure. In another aspect, the other wide-angle XRD peaks in Fig. 2b could be readily indexed to be a pure rhombohedral V_2O_3 (JCPDS card No. 84-0317), which was further verified by the corresponding X-ray photoelectron spectroscopy (XPS) in Fig. S2a. Moreover, taking the results of CHN elemental analysis and inductively coupled plasma atomic emission spectrometry (ICP-AES) in Table S1 into account, the composition of the synthesized sample agreed well with the formula $V_2O_{5.1}C_8H_{8.2}$ (oxygen provided the remaining mass of the sample). The large amount of oxygen reasonably inferred that the organic component in the synthesized sample was phenylacetic acid instead of phenethyl alcohol, which was further confirmed by the corresponding infrared spectroscopy (IR) in Fig. S2b. In this regard, the strong band at 1640 cm^{-1} could be assigned to the stretching vibration of C=O, while the peaks at 1561 cm^{-1} and 1400 cm^{-1} corresponded to the characteristics of the symmetric and asymmetric carboxylic stretching frequencies [21,22], strongly pointing to the oxidation of phenethyl alcohol into phenylacetic acid in our system. In addition, it was found that the carbon/hydrogen ratio fairly agreed with that in the phenylacetate molecules, providing another solid evidence to confirm that only phenylacetate species came from the organic layers. Compared to the experimental value, the slight surplus of hydrogen with respect to phenylacetate inferred the presence of some water adsorbed on the surface [23]. Thus, the composition of the synthesized sample could be split up into $V_2O_{2.5}(C_8H_7O_2)(H_2O)_{0.6}$, which could be further verified by its corresponding thermogravimetric analysis (TGA) in Fig. S3. In this respect, as shown in Fig. S3, the weight loss of ca. 3.2% below 100 °C was primarily due to the release of physically adsorbed water [24], which was well consistent with the calculated 3.6% for the adsorbed water in $V_2O_{2.5}(C_8H_7O_2)(H_2O)_{0.6}$. Another weight loss of ca. 41.29% between 100 °C and 380 °C could be attributed to the combustion of organic phenylacetate species in the layers, which was in good agreement with that calculated from the above formula (46.93%). Interestingly, as shown in Fig. S3, a weight increase took place at above 380 °C, which corresponded to the oxydation of V_2O_3 by trace of oxygen in the N_2 flow [25].

Furthermore, the rod-like structures of rhombohedral V_2O_3 on a gram scale (~1.43 g per one-pot, see Fig. S4a) are depicted by field emission scanning electron microscope (FE-SEM) image in Fig. 2c and transmission electron microscopy (TEM) image in Fig. 2d, displaying a 100% morphological yield of nanorods with widths of ca. 60 nm and lengths up to hundreds of nanometers. More interestingly, the high magnified TEM images in Figs. 2e and S4b clearly revealed that each nanorod exhibited a well-ordered lamellar structure, which was schematically illustrated in Fig. 2f, providing further direct evidence for the formation of mesostruc-

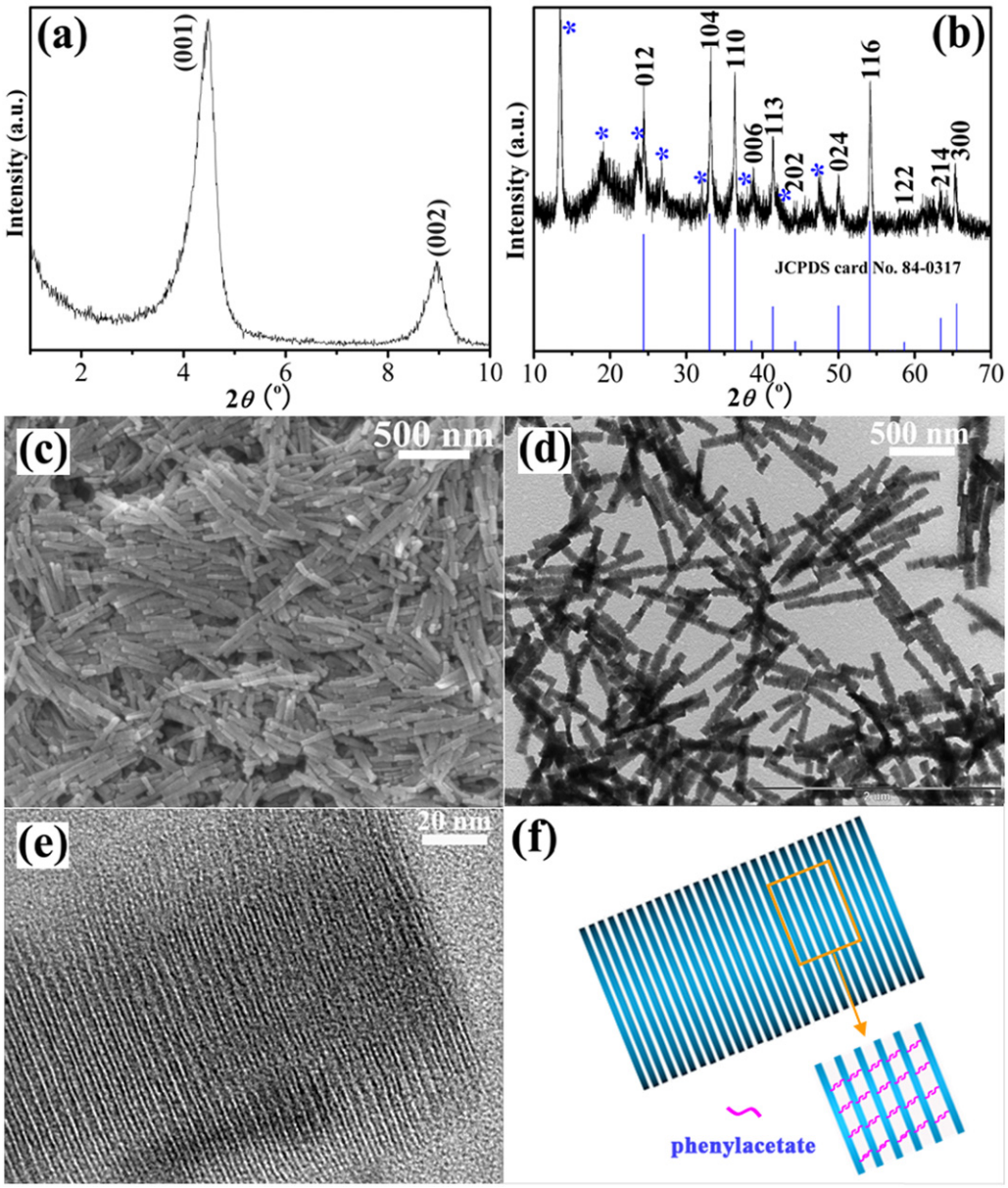

Fig. 2. (a) Small-angle XRD pattern, (b) wide-angle XRD pattern, (c) FE-SEM image, (d) TEM image, (e) high magnified TEM image and (f) corresponding scheme of the as-synthesized highly ordered lamellar V_2O_3-based hybrid nanorods. The ordered mesostructure was also visible on the wide-angle XRD pattern and denoted as asterisk in Fig. 2b.

tured organic–inorganic nanohybrids. Of note, the inorganic layer of rhombohedral V_2O_3 took on an ultrathin sheet-like shape with a thickness of ca. 0.65 nm, while the organic phenylacetate species stayed practically invisible between those layers and possessed a thickness of about 1.3 nm, indicating the presence of double layered phenylacetate molecules interdigitated between the inorganic layers [21,23,26]. As such, the repeat period of this lamellar structure was calculated to be 1.95 nm, which was in excellent agreement with that detected by the small-angle XRD pattern in Fig. 2a. Briefly, all the above results unambiguously determined the gram-scale formation of highly ordered lamellar hybrid nanorods consisting of V_2O_3 crystalline layers with a confined thickness of about 0.65 nm, regularly separated from each other by the organic layers of intercalated phenylacetate molecules.

Motivated by advantages of the fascinating V_2O_3 tunneled crystal structure with intrinsic metallic behavior, the ultrathin sheet-like V_2O_3 layers with confined thickness of 0.65 nm and the highly ordered structures with large interlayer distance of 1.3 nm, herein, we directly introduced these highly ordered lamellar V_2O_3-phenylacetate nanorods as the active material for aqueous lithium-ion battery applications, in efforts to achieve a much higher capacity associated with better capacity retention. As clearly shown in Fig. 3, the charge/discharge curves and corresponding cycle behaviors of these V_2O_3-based hybrid nanorods were compared with those of irregular 10-nm V_2O_3 nanocrystals and 2-μm bulk V_2O_3 (see Figs. S1 and S5). The cells were cycled at a current density of 60 mA g^{-1} with the cutoff voltage of 1.5 and 0.3 V in aqueous electrolyte. It was striking to note that these V_2O_3-based hybrid nanorods exhibited the best electrochemical performance among the above three different structured V_2O_3 (Fig. 3d). As depicted in the insets of Fig. 3a–c, the first discharge capacity of V_2O_3-based hybrid nanorods was up to 131 mAh g^{-1}, which was remarkably

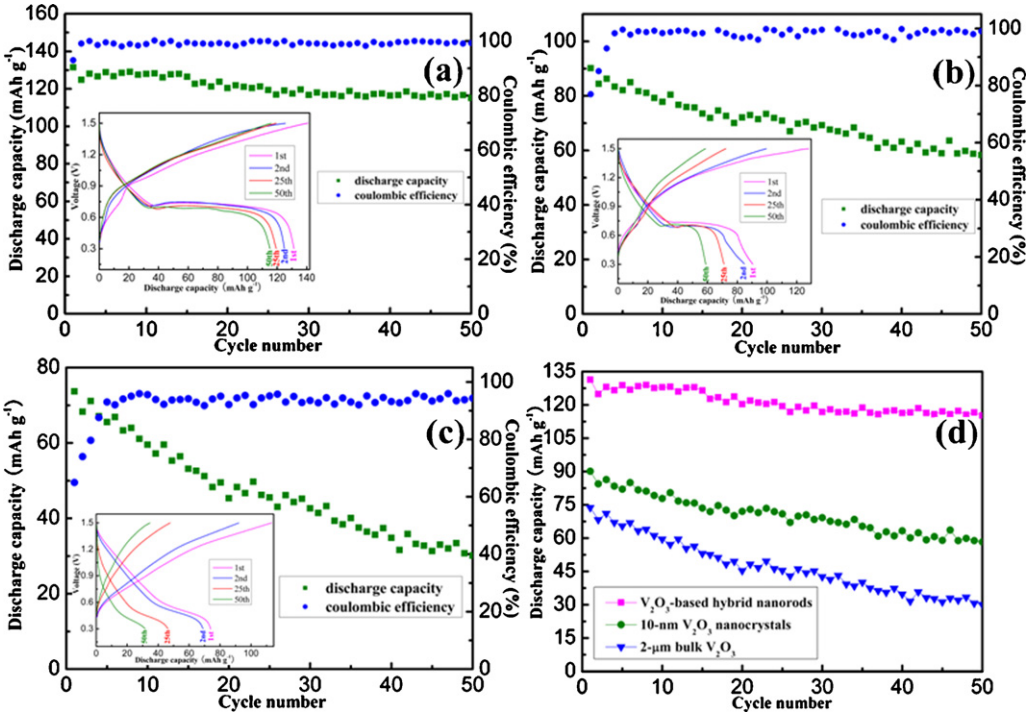

Fig. 3. Discharge capacity and coulombic efficiency versus cycle number curves for the (a) highly ordered lamellar V_2O_3-based hybrid nanorods/$LiMn_2O_4$ cell, (b) 10-nm V_2O_3 nanocrystals/$LiMn_2O_4$ cell and (c) 2-μm bulk V_2O_3/$LiMn_2O_4$ cell in aqueous electrolyte, insets are their corresponding charge and discharge curves at a current density of 60 mA g^{-1} with the cutoff voltage of 1.5 and 0.3 V in aqueous electrolyte; (d) summary of discharge capacity versus cycle number curves for the above three different structured V_2O_3/$LiMn_2O_4$ cells at a current density of 60 mA g^{-1} with the cutoff voltage of 1.5 and 0.3 V in aqueous electrolyte.

(a)

Current density (mA g^{-1})	First discharge capacity (mAh g^{-1})		
	V_2O_3-based hybrid nanorods	10-nm V_2O_3 nanocrystals	2-μm bulk V_2O_3
60	131	90	73.9
120	123.2	77.5	59
180	112.4	65.1	40.8

(c)

Current density (mA g^{-1})	Capacity retention after 50 cycles		
	V_2O_3-based hybrid nanorods	10-nm V_2O_3 nanocrystals	2-μm bulk V_2O_3
60	88%	64%	41%
120	79%	53%	32%
180	70%	41%	20%

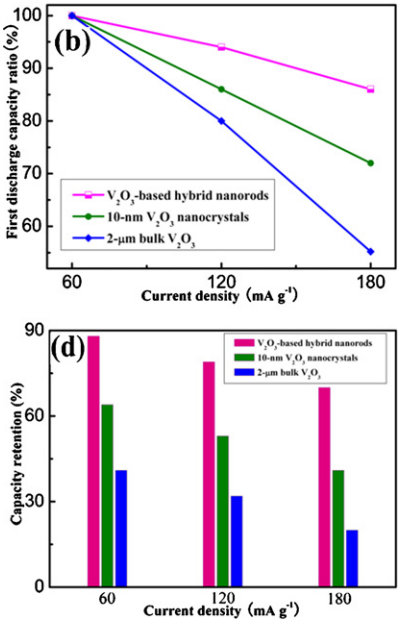

Fig. 4. (a) The effect of current density on the first discharge capacity and (b) the first discharge capacity ratio versus current density curves for V_2O_3-based hybrid nanorods/$LiMn_2O_4$ cell, 10-nm V_2O_3 nanocrystals/$LiMn_2O_4$ cell and 2-μm bulk V_2O_3/$LiMn_2O_4$ cell with the cutoff voltage of 1.5 and 0.3 V in aqueous electrolyte; (c and d) the effect of current density on the capacity retention after 50 cycles for V_2O_3-based hybrid nanorods/$LiMn_2O_4$ cell, 10-nm V_2O_3 nanocrystals/$LiMn_2O_4$ cell and 2-μm bulk V_2O_3/$LiMn_2O_4$ cell with the cutoff voltage of 1.5 and 0.3 V in aqueous electrolyte.

higher than that of 10-nm V_2O_3 nanocrystals and 2-μm bulk V_2O_3 (90 mAh g^{-1} and 73.9 mAh g^{-1}, respectively), indicating that the V_2O_3-based hybrid nanorods possessed more energy density and could discharge a much longer time at the same discharge rate. To the best of our knowledge, the discharge capacity of 131 mAh g^{-1} for the as-synthesized V_2O_3-based hybrid nanorods is strikingly higher than that of most previous aqueous lithium-ion batteries [3–8], enabling this aqueous battery to compete with the conventional organic lithium-ion batteries which usually possess a discharge capacity of ca. 120 mAh g^{-1} [27]. Moreover, as clearly displayed in Fig. 3, the capacity retention of V_2O_3-based hybrid nanorods was as high as 88% after 50 cycles, which was significantly better than that of 10-nm V_2O_3 nanocrystals (64%) and 2-μm bulk V_2O_3 (41%). Very excitingly, it was also found that the cycling

behavior of these V_2O_3-based hybrid nanorods was much superior to most of those in the previously reported aqueous lithium-ion batteries. For example, it was reported that there was only 25 cycles for VO_2(B)/$LiMn_2O_4$ [3], while the capacity retention was down to 40% after 100 cycles for LiV_3O_8/$LiNi_{0.81}Co_{0.19}O_2$ [28], 36% after 100 cycles for LiV_3O_8/$LiCoO_2$ [9], 85% and 75% after 10 cycles for TiP_2O_7/$LiMn_2O_4$ and $LiTi_2(PO_4)_3$/$LiMn_2O_4$ [10], respectively. Furthermore, Fig. 3a–c also revealed that the coulombic efficiency of V_2O_3 electrodes increased gradually and reached a saturated value after cycling several times, which was further confirmed by their corresponding charge/discharge curves in the insets of Fig. 3a–c, implying that the electrochemical systems achieved a state of equilibrium. In addition, the coulombic efficiency of V_2O_3-based hybrid nanorods and 10-nm V_2O_3 nanocrystals remained nearly 100%, which was slightly higher than that of 2-μm bulk V_2O_3 (ca. 95%), revealing their good reversibility during the long-term charge/discharge tests and suggesting that no obvious gas evolution occurred in the cycling voltage region [28]. Of note, as shown in the insets of Fig. 3a–c, one can clearly see that the V_2O_3-based hybrid nanorods and 10-nm V_2O_3 nanocrystals possessed relatively smaller differences in their corresponding charge and discharge profiles than the 2-μm bulk V_2O_3, further verifying their higher coulombic efficiency. Consequently, the above behaviors led to the conclusion that, compared with the nano-sized or bulk V_2O_3, the highly ordered lamellar V_2O_3-based hybrid nanorods performed a remarkably larger discharge capacity and much superior capacity retention, strongly verifying the fascinating superiority of highly ordered lamellar hybrid materials as the aqueous lithium-ion battery electrodes.

In order to further investigate the high-rate performance of these designed highly ordered lamellar V_2O_3-based hybrid nanorods, their electrochemical properties were conducted at different rates ranging from 60 mA g^{-1} to 180 mA g^{-1} and compared with those of 10-nm V_2O_3 nanocrystals and 2-μm bulk V_2O_3 (Fig. 4). Interestingly, for all the above three different structured V_2O_3 electrodes, one can clearly see a decrease in capacity and cyclability with increasing discharge rate, typical of lithium-ion battery electrodes [29]. However, the V_2O_3-based hybrid nanorods still have remarkably larger first discharge capacity than the 10-nm V_2O_3 nanocrystals and 2-μm bulk V_2O_3 at high discharge rates, as illustrated in Fig. 4a and b. For example, at the discharge rate up to 180 mA g^{-1}, the V_2O_3-based hybrid nanorods still retained a first discharge capacity of 112.4 mAh g^{-1}, corresponding to 86% of that at 60 mA g^{-1}, while the 10-nm V_2O_3 nanocrystals and 2-μm bulk V_2O_3 only delivered 65.1 mAh g^{-1} and 40.8 mAh g^{-1} which corresponded to 72% and 55% of their capacity at 60 mA g^{-1}, respectively. Especially notable is the excellent high-rate capability of the V_2O_3-based hybrid nanorods behaving the capacity retention of 70% at the high discharge rate of 180 mA g^{-1}, whereas the 10-nm V_2O_3 nanocrystals and 2-μm bulk V_2O_3 only showed very poor capacity retention of 41% and 20% (Fig. 4c and d), respectively. Obviously, the unique structure form of V_2O_3-based hybrid nanorods contributed to their significantly faster kinetic properties than the 10-nm V_2O_3 nanocrystals and 2-μm bulk V_2O_3 at high current rates.

Notably, the eminently improved electrochemical properties especially the high-rate performances of these V_2O_3-based hybrid nanorods could be ascribed to the synergistic effect between their microscopic tunneled crystal structure and macroscopic morphological features of ultrathin sheet-like V_2O_3 layers and highly ordered interlayer structures. Intriguingly, the extremely thin V_2O_3 sheets with thickness of 0.65 nm as well as the intrinsically tunneled crystal structure would not only help to strikingly shorten the lithium ion diffusion length but also provide a greatly increased surface area contact with electrolyte, thus contributing to achieve faster kinetics and higher capacity [12,13,30,31]. Analogously, benefited from the short lithium ion diffusion length and large contact area with electrolyte, the 10-nm V_2O_3 nanocrystals also delivered a much higher capacity than the 2-μm bulk V_2O_3 (90 mAh g^{-1} versus 73.9 mAh g^{-1}), further implying the charming superiority of ultrathin V_2O_3 sheets within the hybrid nanorods. In addition, the periodic lamellar structure was kept together by simple π–π interactions between phenyl rings [23,26], which allowed for efficient transport of electrons and lithium ions along the 1D hybrid nanorods and hence favored for acquiring rapider lithium kinetics and better cycling [12,14,32]. By the contrary, as for the 10-nm V_2O_3 nanocrystals and 2-μm bulk V_2O_3, the electrons and lithium ions must move through the disconnected particles, which unfortunately increased their transport path and hence resulted in their poor electrochemical performances, especially when the batteries were cycled under high discharge rates (Fig. 4). Moreover, it was noticeable that the interlayer distance of ca. 1.3 nm, which was significantly larger than the diameter of lithium ion (0.136 nm), not only facilitated the electrolyte penetrate into the inner part of active materials but also provided abundant space for the intercalation of lithium ions [16,17,33], further helping to improve the lithium diffusion kinetics and storage capacity. That was to say, compared with the 10-nm V_2O_3 nanocrystals and 2-μm bulk V_2O_3, the extra discharge capacity of the V_2O_3-based hybrid nanorods mainly came from the deintercalation of lithium ions stored in the large interlayer space. Furthermore, it was well-known that the intercalation of lithium ions into the active materials inevitably caused its volume expansion, pulverization and shedding, which gradually led to its capacity fading [14,34]. As for our synthesized V_2O_3-based hybrid nanorods, the presence of highly ordered interlayer structure was expected to buffer well against the volume expansion of the ultrathin V_2O_3 layers during lithium intercalation/deintercalation, thus ensuring good electrical contact with the electrode and hence improving their cycling behavior [16]. In this regard, after the electrochemical performance was performed, the phase and morphology of V_2O_3-based hybrid nanorods were re-investigated by means of XRD, SEM and TEM measurements, as displayed in Fig. S6. The results showed that the structure of highly ordered lamellar hybrid nanorods as well as the phase of rhombohedral V_2O_3 preserved quite well after repeated charge/discharge processes. Then the whole electrochemical reaction can be described by the following equation:

$$V_2O_3 + \chi Li^+ + \chi e^- \underset{\text{discharge}}{\overset{\text{charge}}{\rightleftharpoons}} Li_\chi V_2O_3 \quad (1)$$

Likewise, owing to the better ability to tolerate volume expansion, the 10-nm V_2O_3 nanocrystals also performed much improved cyclability than the 2-μm bulk V_2O_3, which indirectly inferred the unique advantage of highly ordered interlayer structures in accommodating volume change.

4. Conclusions

In conclusion, we first put forward a novel and ideal model system of ordered lamellar organic–inorganic hybrid nanorods as an excellent platform to greatly enhance the capacity and cyclability of aqueous lithium-ion batteries. Then, a facile non-aqueous route is developed to realize the gram-scale synthesis of highly ordered lamellar hybrid nanorods consisting of ultrathin V_2O_3 layers with thickness of ca. 0.65 nm, regularly separated from each other by organic phenylacetate layers. As expected, these V_2O_3 nanorods deliver a capacity up to 131 mAh g^{-1}, nearly 1.5 and 2 times higher than that of 10-nm V_2O_3 nanocrystals (90 mAh g^{-1}) and 2-μm bulk V_2O_3 (73.9 mAh g^{-1}). Also, they exhibit excellent capacity retention of 88% after 50 cycles, remarkably better than that of 10-nm V_2O_3 nanocrystals (64%) and 2-μm bulk V_2O_3 (41%). Notably, the strikingly improved capacity, cyclability and rate capability could be ascribed to the synergetic effect between

their microscopic tunneled crystal structure and macroscopic morphological features of ultrathin V_2O_3 layers and highly ordered interlayer structures. These structural features help to provide easy electrolyte infiltration, efficient 1D transport pathway, large contact area with electrolyte, short diffusion length and extra storage space for lithium ions as well as sufficient interlayer space to buffer volume expansion. Briefly, this work not only provides a high-yield route for synthesizing highly ordered lamellar hybrid materials but also proves that these unique structures are excellent platforms for improving the aqueous lithium-ion battery performances especially at high discharge rates. It is anticipated that this present study may open new avenues towards the rational design and synthesis of other ordered lamellar organic–inorganic hybrid materials, which can be applicable to aqueous lithium-ion batteries and energy storage applications.

Acknowledgments

This work was financially supported by National Basic Research Program of China (2009CB939901) and National Nature Science Foundation (90922016, 10979047, 11079004).

Appendix A. Supplementary data

Supplementary data associated with this article can be found, in the online version, at doi:10.1016/j.jpowsour.2011.06.050.

References

[1] B. Scrosati, Nature 373 (1995) 557.
[2] M. Broussely, J.P. Planchat, G. Rigobert, D. Virey, G. Sarre, J. Power Sources 68 (1997) 8.
[3] W. Li, J.R. Dahn, D. Wainwright, Science 264 (1994) 1115.
[4] G.J. Wang, Q.T. Qu, B. Wang, Y. Shi, S. Tian, Y.P. Wu, ChemPhysChem 9 (2008) 2299.
[5] C.Z. Wu, Z.P. Hu, W. Wang, M. Zhang, J.L. Yang, Y. Xie, Chem. Commun. (2008) 3891.
[6] S.D. Zhang, Y.M. Li, C.Z. Wu, F. Zheng, Y. Xie, J. Phys. Chem. C 113 (2009) 15058.
[7] J.Y. Luo, W.J. Cui, P. He, Y.Y. Xia, Nat. Chem. 2 (2010) 760.
[8] J.Y. Luo, Y.Y. Xia, Adv. Funct. Mater. 17 (2007) 3877.
[9] G.J. Wang, L.J. Fu, N.H. Zhao, L.C. Yang, Y.P. Wu, H.Q. Wu, Angew. Chem. Int. Ed. 46 (2007) 295.
[10] H.B. Wang, K.L. Huang, Y.Q. Zeng, S. Yang, L.Q. Chen, Electrochim. Acta 52 (2007) 3280.
[11] C.R. Kagan, D.B. Mitzi, C.D. Dimitrakopoulos, Science 286 (1999) 945.
[12] E. Hosono, T. Kudo, I. Honma, H. Matsuda, H.S. Zhou, Nano Lett. 9 (2009) 1045.
[13] J.H. Liu, J.S. Chen, X.F. Wei, X.W. Lou, X.W. Liu, Adv. Mater. 23 (2011) 998.
[14] C.K. Chan, H. Peng, G. Liu, K. Mcllwrath, X.F. Zhang, R.A. Huggins, Y. Cui, Nat. Nanotechnol. 3 (2008) 31.
[15] C.K. Chan, X.F. Zhang, Y. Cui, Nano Lett. 8 (2008) 307.
[16] Y.F. Shi, B.K. Guo, S.A. Corr, Q.H. Shi, Y.S. Hu, K.R. Heier, L.Q. Chen, R. Seshadri, G.D. Stucky, Nano Lett. 9 (2009) 4215.
[17] M. Nakayama, M. Shamoto, A. Kamimura, Chem. Mater. 22 (2010) 5887.
[18] J.W. Taylor, T.J. Smith, K.H. Andersen, H. Capellmann, R.K. Kremer, A. Simon, O. Schärpf, K.U. Neumann, K.R.A. Ziebeck, Eur. Phys. J. B 12 (1999) 199.
[19] A. Tranchant, R. Messina, J. Perichon, J. Electroanal. Chem. 13 (1980) 225.
[20] H.M. Liu, Y.G. Wang, H.Q. Li, W.S. Yang, H.S. Zhou, ChemPhysChem 11 (2010) 3273.
[21] N. Pinna, G. Garnweitner, P. Beato, M. Niederberger, M. Antonoetti, Small 1 (2005) 112.
[22] J. Polleux, N. Pinna, M. Antonietti, M. Niederberger, J. Am. Chem. Soc. 127 (2005) 15595.
[23] M. Karmaoui, L. Mafra, R.A. Sá Ferreira, J. Rocha, L.D. Carlo, N. Pinna, J. Phys. Chem. C 111 (2007) 2539.
[24] L.L. Zhang, W.G. Zhang, L. Lu, X.J. Yang, X. Wang, J. Mater. Sci. 41 (2006) 3917.
[25] F. Sediri, N. Hgarbi, Mater. Sci. Eng. B 123 (2005) 136.
[26] M. Karmaoui, R.A. Sá Ferreira, A.T. Mane, L.D. Carlos, N. Pinna, Chem. Mater. 18 (2006) 4493.
[27] M. Okubo, E. Hosono, J. Kim, M. Enomoto, N. Kojima, T. Kudo, H. Zhou, I. Honma, J. Am. Chem. Soc. 129 (2007) 7444.
[28] J. Köhler, H. Makihara, H. Uegaito, H. Inoue, M. Toki, Electrochim. Acta 46 (2000) 59.
[29] C.Z. Wu, Y. Xie, L.Y. Lei, S.Q. Hu, C.Z. OuYang, Adv. Mater. 18 (2006) 1727.
[30] H.S. Zhou, D.L. Li, M. Hibino, I. Honma, Angew. Chem. Int. Ed. 44 (2005) 797.
[31] Y. Xu, L. Zheng, Y. Xie, Dalton Trans. 39 (2010) 10729.
[32] H.W. Lee, P. Muralidharan, R. Ruffo, C.M. Mari, Y. Cui, D.K. Kim, Nano Lett. 10 (2010) 3852.
[33] X.W. Lou, C.M. Li, L.A. Archer, Adv. Mater. 21 (2009) 2536.
[34] Q.F. Zhang, W.X. Zhang, W.H. Wan, Y. Cui, E. Wang, Nano Lett. 10 (2010) 3243.